Ocean Engineering 243 (2022) 110225

Contents lists available at ScienceDirect

Ocean Engineering

journal homepage: www.elsevier.com/locate/oceaneng

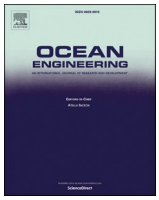

Numerical investigations into the ventilation elimination mechanism of a surface-piercing hydrofoil

Yuchang Zhi [a], Jiemin Zhan [a], Renfang Huang [b,**], Rundi Qiu [b,c], Yiwei Wang [b,c,*]

[a] School of Aeronautics and Astronautics, Department of Applied Mechanics and Engineering, Sun Yat-Sen University, Guangzhou, 510275, China
[b] Key Laboratory for Mechanics in Fluid Solid Coupling Systems, Institute of Mechanics, Chinese Academy of Sciences, Beijing, 100190, China
[c] School of Engineering Science, University of Chinese Academy of Sciences, Beijing, 100049, China

ARTICLE INFO

Keywords:
Surface-piercing hydrofoil
Ventilation elimination
Re-entrant jet
RANS

ABSTRACT

This paper investigates the ventilation elimination mechanisms during the deceleration process of a surface-piercing hydrofoil using the unsteady Reynolds-averaged Navier-Stokes (RANS) method together with a Volume of Fluid (VOF) model. The numerical results are in good agreement with the experimental data. The ventilation elimination mechanism of the surface-piercing hydrofoil is analyzed from the perspectives of the hydrofoil hydrodynamic performance, the ventilated cavity evolution, vortex structures, and re-entrant jets. The results indicate that the ventilation elimination includes three stages, i.e. a decrease in the ventilated cavity, washout, and reattachment. The decrease in the ventilated cavity is due to the hydrofoil speed decrease in the FV flow. Washout is the transition from fully ventilated to partially ventilated flow, and reattachment is the transition from partially ventilated to fully wetted flow. The underwater vortex structures around the surface-piercing hydrofoil are composed of a tip vortex, an unstable vortex induced by the shear layer, and a Karman vortex caused by the vortex shedding from the trailing edge of the hydrofoil. Ventilation stability strongly depends on the re-entrant jet. When Φ (the angle between the flow direction and the closure line of the ventilated cavity) is greater than 45°, the re-entrant jet impinges on the ventilated cavity's leading edge and destabilizes the ventilated cavity.

1. Introduction

Atmospheric ventilation affects the performance of many hydraulic devices, such as propellers, rudders, and hydrofoils, when they work near the free surface (Arndt et al., 2009; Korulla and Sha, 2012). On the one hand, under certain conditions, ventilation can improve the stability and efficiency of some hydraulic devices, such as surface-piercing propellers (Califano and Steen, 2009; Yousefi and Shafaghat, 2020). On the other hand, partial ventilation causes instability and reduces their hydrodynamic performance due to the air ingression into the low-pressure areas (Matveev et al., 2019). Therefore, it is great of importance to investigate the formation, disappearance, stability and controllability of atmospheric ventilation (Damley-Strnad et al., 2019; Rood Jr, 1975).

Since 1950, lots of scholars have conducted systematic experiments on the ventilation (Ashworth Briggs et al., 2014; Harwood et al., 2019, 2020; Metcalf et al., 2006; Shen and Wermter, 1979). Wetzel (1957) carried out ventilation experiments for vertical struts of different shapes, and they found that atmospheric ventilation is mainly related to velocity, yaw angle, immersion depth, and strut shape. Rothblum (1977) conducted experiments around vertical struts and found different ventilation patterns, such as ventilation at the trailing edge, and natural cavitation-ventilation. At the same time, a ventilation-suppression experiment was carried out to control the ventilation. Early experimental research mostly focused on various ventilation patterns but did not determine the relationships between them. In recent years, Young et al. (2013) and Harwood et al. (2016) carried out a detailed series of ventilation experiments at low-to-moderate Froude numbers and proposed a mechanism of ventilation formation and disappearance. Fully ventilated (FV), partially ventilated (PV), and fully wetted (FW) flow regimes were established, and their stable regions were described as parametric spaces. The stability of fully and partially ventilated regimes was connected to the re-entrant jet's angle, and the re-entrant jet is used

* Corresponding author. Key Laboratory for Mechanics in Fluid Solid Coupling Systems, Institute of Mechanics, Chinese Academy of Sciences, Beijing, 100190, China.
** Corresponding author.
E-mail address: wangyw@imech.ac.cn (Y. Wang).

https://doi.org/10.1016/j.oceaneng.2021.110225
Received 6 April 2021; Received in revised form 16 November 2021; Accepted 17 November 2021
Available online 25 November 2021

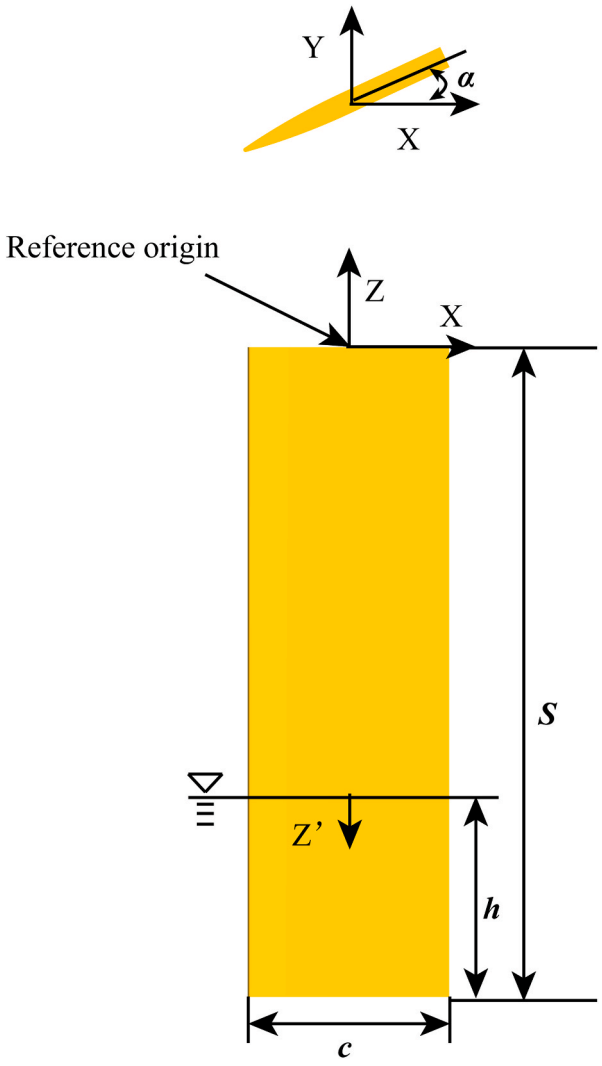

Fig. 1. Hydrofoil geometry model.

to evaluate the various flow regimes. Brizzolara and Young (2012) designed a new type of supercavitating surface-piercing hydrofoil (Brizzolara and Federici, 2011; Brizzolara and Villa, 2012) by using numerical simulations with the hydrofoil pressure side obtained by the Tulin and Johnson's method (Tulin and Burkart, 1955). And the supercavitating surface-piercing hydrofoil performed good hydrodynamic characteristics at high and low cavitation numbers. Ventilation experiments on a 1/6 scale model of a three-dimensional hydrofoil (Charlou and Wackers, 2019; Vernengo et al., 2016) were carried out in a free-surface cavitation tunnel at the Technical University of Berlin (TUB), and the natural cavitation–ventilated flow at low cavitation number was observed.

Ventilation is a type of multiphase flow characterized by the entrainment of noncondensable gas into the liquid flow around a fully or partially immersed body. Traditional ventilation experiments can only observe the shape of the ventilated cavity and the macroscopic force of the hydrodynamic device, but it is difficult to observe flow distribution near the device or inside the ventilated cavity. With the development of computer science and technology, computational fluid dynamics (CFD) has been used to simulate the ventilation phenomena for various hydraulic devices (Andrun et al., 2021; Barden and Binns, 2012; Matveev et al., 2018; Ungureanu and Lungu, 2010). Vernengo et al. (2016) and Charlou and Wackers (2019) used the Reynolds-averaged Navier-Stokes (RANS) solver and the Schnerr–Sauer (S–S) cavitation model to solve the flow of a mixture of air/steam and water phases, yielding a good agreement with experimental results. The suction side of the surface-piercing propeller usually works in three phases, i.e. air, water and cavitation, so the ventilation and cavitation modes play an important role in the propeller's hydrodynamic performance. Andrun et al. (2021) discussed the effects of different numerical schemes (i.e. the turbulent intensity, time-step, interface capture scheme) to capture the ventilation phenomenon of a surface-piercing hydrofoil, and finally found that a reasonable time-step and mesh are conducive to predicting the ventilated flow features. Xu et al. (2017) and Wang et al. (2016) used a horizontal-transmitter mechanism in an experimental cavitation system to carry out a large number of cavitation experiments on rotating bodies and vertical hydrofoils near free surfaces. The calculations were in good agreement with results under typical experimental conditions, and the results show that the characteristics of the re-entrant jet and cavitation shedding are closely related to the distance from the free surface.

As the above literature review indicates, it is difficult to experimentally visualize the flow fields near/within the ventilated cavities, and most of the recent numerical simulations are concentrated upon the steady-state ventilation. A few studies have been studied on the formation and elimination of atmospheric ventilation, so it is necessary to shed light on these processes further by using the numerical approach. In this paper, the deceleration process of a surface-piercing hydrofoil is numerically simulated using the RANS and a VOF model. The emphasis is to clarify the ventilation elimination mechanism from various perspectives of the foil hydrodynamic performance, ventilated cavity evolution, vortex structures and re-entrant jets.

2. Computational approach

A state-of-the-art RANS solver with VOF (Matveev et al., 2018) method was chosen to describe the free surface. It is incorporated into a software suite (CD-Adapco, 2012) that can model full-scale turbulent flow around an object under non-stationary conditions. The VOF model uses a simplified adiabatic cavitation model to predict the free surface as described in the next paragraph.

The solver is applied to the following set of equations that express the mass and momentum equilibrium in the Eulerian framework and the Reynolds-averaged approach with the necessary boundary conditions. The RANS equations for an incompressible flow are shown in Equation (1):

$$\begin{cases} \nabla\cdot\mathbf{U} = 0 \\ \rho\mathbf{V} = -\nabla P + \mu\Delta\mathbf{V} + \nabla\cdot\mathrm{T}_{Re} + \mathbf{S}_M \end{cases} \tag{1}$$

where $\mathbf{U}$ is the Reynolds-averaged flow velocity vector, T_{Re} is the Reynolds stress tensor, P is the averaged pressure, $\mathbf{S}_M$ is the momentum source vector, and μ is the dynamic viscosity. The components of the Reynolds stress tensor are closured with the realizable k-ε turbulence model based on the Boussinesq hypothesis:

$$\mathrm{T}_{ij}^{Re} = \mu_t\left(\frac{\partial\mathbf{V}_i}{\partial x_j} + \frac{\partial\mathbf{V}_j}{\partial x_i}\right) - \frac{2}{3}\rho k\delta_{ij} = 2\mu_t\mathrm{D}_{ij} - \frac{2}{3}\rho k\delta_{ij} \tag{2}$$

where k is the turbulent kinetic energy, and μ_t is the turbulent viscosity.

As regards the wall function, on the cell closest to the profile, a two layer model approach has been applied. The two layer wall function model is a model that imposes a first thin laminar layer near the wall and a second logarithmic layer over the first, and this model assumes that the centroid of the first cell near the wall lies within the logarithmic region of the boundary layer. A much smaller value of wall distance y + has been used in this study in order to accurately solve the cavity thickness growth along the wall.

Table 1
Geometric parameters of hydrofoil.

Chord length	c	0.2794m
Foil span	S	0.8382m
Tip immersion	h	0.2794m
Immersed aspect ratio	$AR_h = \frac{h}{c}$	1
Velocities	U_∞	0–4.13 m/s
Depth Froude number	$F_{nh} = \frac{U_\infty}{\sqrt{gh}}$	0–2.5
Attack angle	α	25°

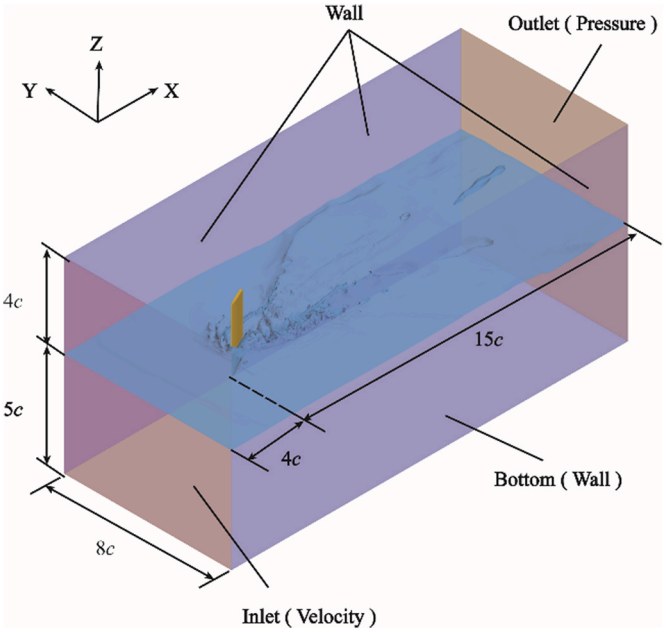

Fig. 2. Computational domain and boundary conditions.

3. Verification and Validation

3.1. Simulation setup

A symmetrical hydrofoil was selected as the research object, as shown in Fig. 1. Harwood et al. (2016) conducted a series of experiments on the hydrodynamic performance and flow regimes of the hydrofoil. The calculation model is the same as the experimental model, as shown in Table 1.

Fig. 2 shows the computational domain and boundary conditions. The ranges of the computational domain in the X, Y and Z directions are [-4c, 15c], [-4c, 4c] and [-5c, 4c], respectively, where c is the chord length. The inlet condition is set as the velocity inlet, the outlet condition is set as the pressure outlet, and the other boundaries are set as the walls. The time-step is set to 0.001s, which is validated to meet the requirements for most hydrofoil ventilation calculations by Harwood et al. (2014) and Andrun et al. (2021).

3.2. Mesh generation and refinement

In ventilation simulations, mesh quality and resolution affect predictions of a ventilated cavity. High-quality Cartesian grids are generated by STAR-CCM + software. To accurately capture the ventilated cavity details, the control volume method was used to appropriately refine the spray regions, the tip vortex region and the ventilated cavity region, as shown in Fig. 3(a). The mesh around the hydrofoil is shown in Fig. 3(b), and most cells have quite good orthogonality and are of high quality. Moreover, $y+$ is always less than 1, and the boundary layer is set to be 20 layers. The mesh in the boundary layer around the hydrofoil was carefully generated to fulfill the requirements of the wall function.

3.3. Mesh verification

Mesh refinement helps to improve the calculation accuracy of the ventilated cavity. According to the uncertainty research method, three grids are created to perform uncertainty analysis (Yuan and Xing, 2016), and the refinement ratio of the mesh is defined by:

$$r = \left(\frac{N_{\text{fine}}}{N_{\text{coarse}}}\right)^{1/d} \tag{3}$$

where d is the dimension of the problem explored and N is the total number of cells in the simulation. In this study, we considered a three-dimensional problem ($d = 3$). The refinement ratio of meshes in this study was approximately 1.2. The lift coefficient C_L and drag coefficientC_D of the hydrofoil were calculated under the working conditions $F_{nh} = 2.5$, $AR_h = 1.0$, $\alpha = 25^\circ$. The lift coefficient C_L and drag coefficientC_D are defined by:

$$C_L = \frac{L}{0.5\rho U_\infty^2 hc},\ C_D = \frac{D}{0.5\rho U_\infty^2 hc} \tag{4}$$

The grid number and the hydrofoil hydrodynamic performance are shown in Table 2. Take the coarse mesh as an example, the relative error

Table 2
Mesh number and hydrofoil hydrodynamic performance.

	ID	Grid volume	C_L-mean	Error (%)	C_D-mean	Error (%)
Exp			0.42		0.23	
Fine	S1	734M	0.434	3.33	0.239	3.91
Medium	S2	1066M	0.433	3.10	0.240	4.35
Coarse	S3	1713M	0.435	3.57	0.242	5.22

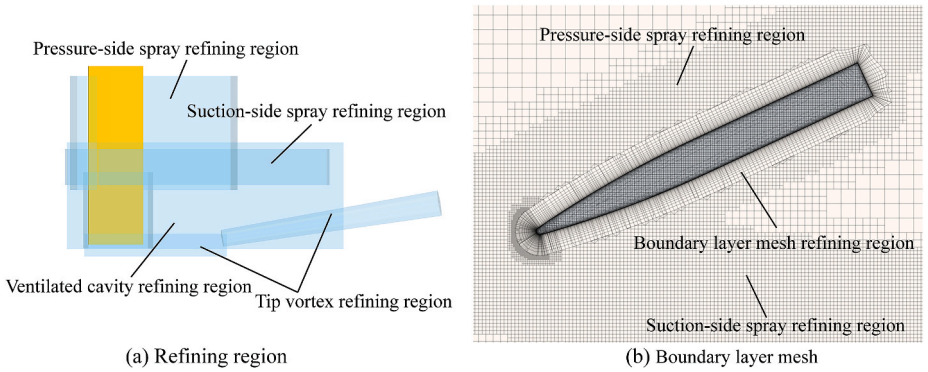

(a) Refining region (b) Boundary layer mesh

Fig. 3. Meshing details.

Table 3
Uncertainty analysis parameters.

	e_{12}	e_{23}	R_G	P_G	U_G
C_L	0.001	0.002	0.5	1.9	0.016
C_D	0.001	0.002	0.5	1.9	0.016

is 3.57% for the lift coefficient and 5.22% for the drag coefficient, when compared to the experiments, which demonstrates that the present numerical approach meets the requirements for engineering applications. Table 3 shows the uncertainty analysis parameters. The grid convergence rate R_G is less than 1, so the calculated C_L andC_D converge monotonically with an increase in the number of grids. The results show that uncertainty of C_L and C_D, estimated by Roache and Stern's method (Roache, 1997; Stern et al., 2006; Wang et al., 2018), is less than 5%, which demonstrates that the present simulations are almost independent of the grid resolution.

Comparisons of the ventilated cavity between calculations and experiments are shown in Fig. 4. The coarse, medium and fine grids satisfactorily represent the experimental ventilation flow regime, especially the tip vortex formation. The grid refinement helps to precisely capture the detailed flow features, such as splashes on free surfaces and the ventilated cavity shapes. Considering the computational cost and numerical stability, the medium mesh was fully capable of numerical simulations in this study, and therefore it was used for all computations.

4. Results and discussion

4.1. Hydrodynamic performance of the surface-piercing hydrofoil

The ventilation elimination mechanisms and stability of a surface-piercing hydrofoil were analyzed based on hydrofoil hydrodynamic performance and cavity ventilation during the deceleration process. The moving velocity profile of the hydrofoil is extracted from the experiment and then applied as the inlet boundary condition in the numerical simulation. The hydrofoil sailed at constant speed of $F_{nh} = 2.5$, and when the ventilated cavity and hydrodynamic performance stabilized, the hydrofoil decelerated linearly (Harwood et al., 2014). Fig. 5 shows two different deceleration trends, namely speed1 is consistent with the experiment, and for comparison, speed2 has a greater deceleration slope.

It can be seen from Fig. 6 that during hydrofoil deceleration, the calculated hydrodynamic performance was in good agreement with the experiment. The hydrofoil hydrodynamic performance has a strong correlation with the moving velocity. The lift and drag of the hydrofoil decrease with the speed of the hydrofoil decreases.

The effect of the speed profile on the lift and drag coefficients is

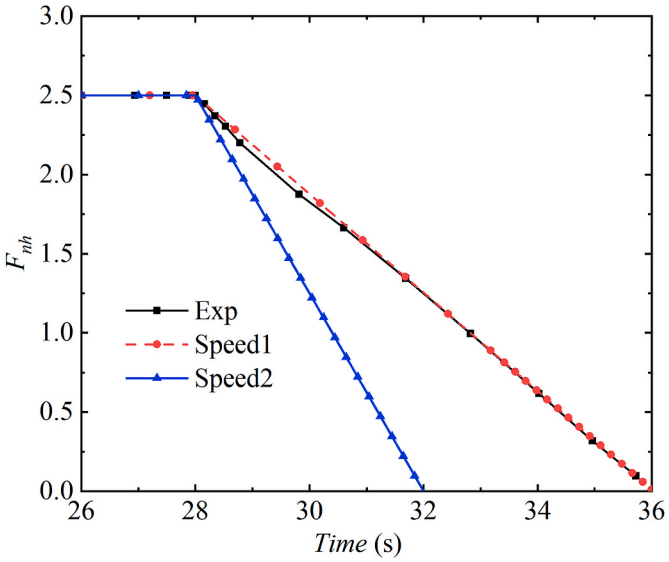

Fig. 5. Time histories of velocity.

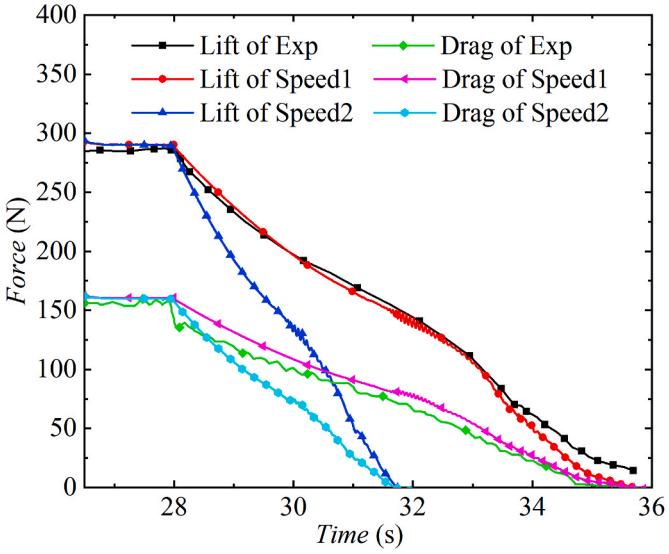

Fig. 6. Time history of lift and drag.

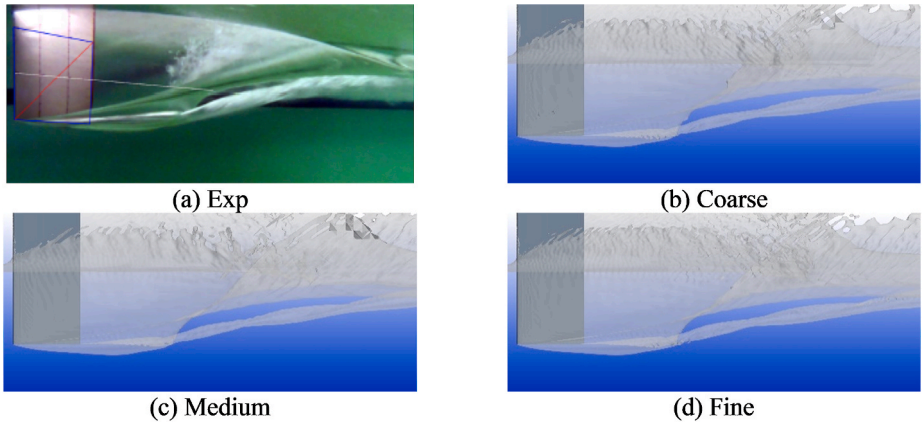

Fig. 4. Comparison of calculation results and experiments.

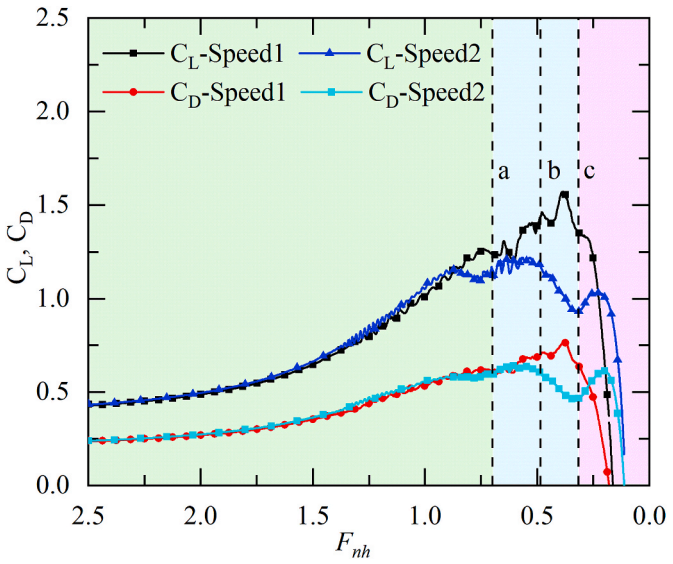

Fig. 7. The effect of the speed profile on the lift and drag coefficient. (The dashed vertical line labeled ('a') indicates $F_{nh} = 0.695$, the line ('b') indicates $F_{nh} = 0.484$, and the line ('c') indicates $F_{nh} = 0.309$.).

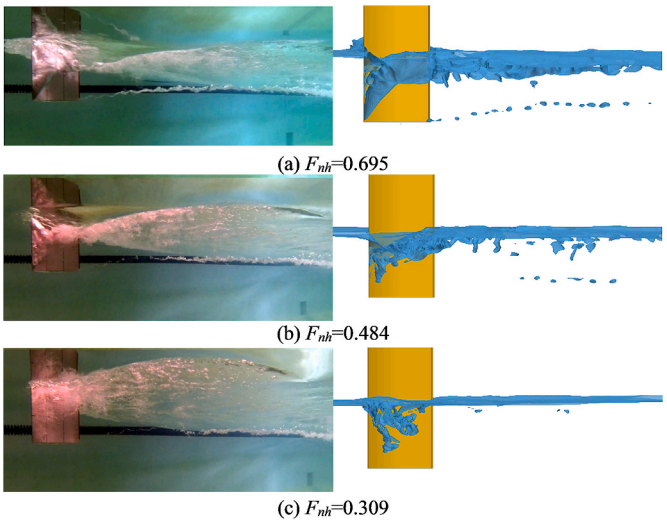

Fig. 8. Experimental and calculated flow characteristics of the ventilated cavity at typical instants.

shown in Fig. 7. For speed 1, it can be seen that the lift coefficient and drag coefficient of the hydrofoil decrease with the hydrofoil speed decreases in the fully wetted flow regime, while the lift coefficient and drag coefficient of the hydrofoil increase with in the fully ventilated flow state. This is mainly ascribed to the fact that ventilation changes the pressure distribution on the hydrofoil suction surface and reduces the hydrofoil performance. In the partially ventilated flow regime, the lift coefficient and drag coefficient of the hydrofoil are more unsteady, which is caused by the instability of the ventilated cavity at the hydrofoil suction surface. When it comes to speed2, it exhibits a partial drop and a small secondary hump in C_L and C_D. This can be attributed to the faster deceleration and the more intense wake memory effect at speed2, which delays return to partially ventilated (PV) flow and fully wetted (FW) flow. For speed 1, as the Froude number decreases, the ventilated cavity starts to fall off in the streamwise direction and the hydrofoil suction surface is reattached by the water fluid. For speed 2, the ventilated cavity is difficult to fall off and remains in the place at lower speeds, compared to the speed1 case. The unshed ventilated cavity changes the pressure distribution on the suction-surface, which reduces the pressure difference between the pressure surface and the suction surface of the hydrofoil. Therefore, there is a local drop in the lift and drag coefficient for speed 2. As the ventilated cavity starts to fall off in the streamwise direction, it follows that the hydrofoil C_L and C_D increase and the small secondary hump appear. It should be noted that when F_{nh}<0.5, the denominators of $C_L = L/0.5\rho U_\infty^2 hc$ are vanishingly small, so any noise in the signal is amplified. This could cause erroneous lift coefficient and drag coefficient results. Therefore, in the future, we need to conduct a detailed analysis of the differences between the two speed profiles.

Three flow regimes are observed during the hydrofoil deceleration process, that is, fully ventilated (FV) flow, partially ventilated (PV) flow and fully wetted (FW) flow. Fully ventilated (FV) flow is defined as the case when a cavity is entrained along the entire immersed span of the hydrofoil's suction surface and there is no inherently-destabilizing re-entrant jet. Partially ventilated (PV) flow is defined as the state that the ventilated cavity neither covers the entire immersed portion of the hydrofoil nor meets the stability conditions to sustain fully ventilated flow. Fully wetted (FW) flow is defined as the regime that there is no pronounced gas entrainment.

As for speed 1, the dashed vertical line labeled ('a') in Fig. 7 indicates the time in Fig. 8(a) when the flow was transitioning from FV to PV at the moment of the initial washout, the line ('b') indicates a typical period of PV illustrated in Fig. 8 (b), and the line ('c') indicates the time in Fig. 8 (c) when the flow was changing from PV to FW at the moment of reattachment.

Fig. 8 shows the experimental (left panels) and calculated (right panels) flow regimes of the ventilated cavity at typical instants. The calculations capture the flow characteristics, especially formation of the tip vortex under different flow regimes. Next mainly discussed the ventilation elimination process at speed 1.

4.2. Evolution of flow patterns in the ventilated cavities

Fig. 9 shows the ventilated cavity evolution of a surface-piercing hydrofoil during the deceleration process. It can be seen that the evolution is a process of the ventilated cavity reducing, companied by the water reattachment to the hydrofoil suction surface. Three stages can describe the disappearance of the ventilated cavity:

(1) A decrease in the ventilated cavity: During this stage, the length of the ventilated cavity on the hydrofoil's suction surface becomes shorter, the spray formed by the pressure gradient on both hydrofoil sides gradually decreases, and the tip vortex cavity gradually decreases. Simultaneously, the angle between the closure line of the ventilated cavity and the flow direction gradually increases as the re-entrant jet moves toward the leading edge of the hydrofoil. As the F_{nh} decreases from Fig. 9 (a)–(e), the cavitation number increased gradually, causing a decrease in the ventilated cavity length. Meanwhile, the reason for the tip vortex decrease is that the low-pressure region is difficult to supplement air from the ventilated cavity. The ventilated cavity is relatively stable during this stage, which mainly because the angle Φ (between the closure line of the ventilated cavity and the flow direction) showing in Fig. 9 is less than 45° ($\Phi < 45°$).
(2) Washout: Washout describes the transition from FV to PV flow, which is shown in Fig. 9(e) and (f), when the cavity closure line exceeds the 45° criterion ($\Phi \geq 45°$). Washout is a discrete event that occurs inception of ventilated cavity instability caused by the re-entrant jet. When $\Phi \geq 45°$, the re-entrant jet impinges on the leading edge of the ventilated cavity with sufficient upstream momentum, it follows by the destabilization of the ventilated cavity.
(3) Reattachment: Reattachment describes the transition from PV to FW flow, which is shown in Fig. 9(g and h). During this stage, the

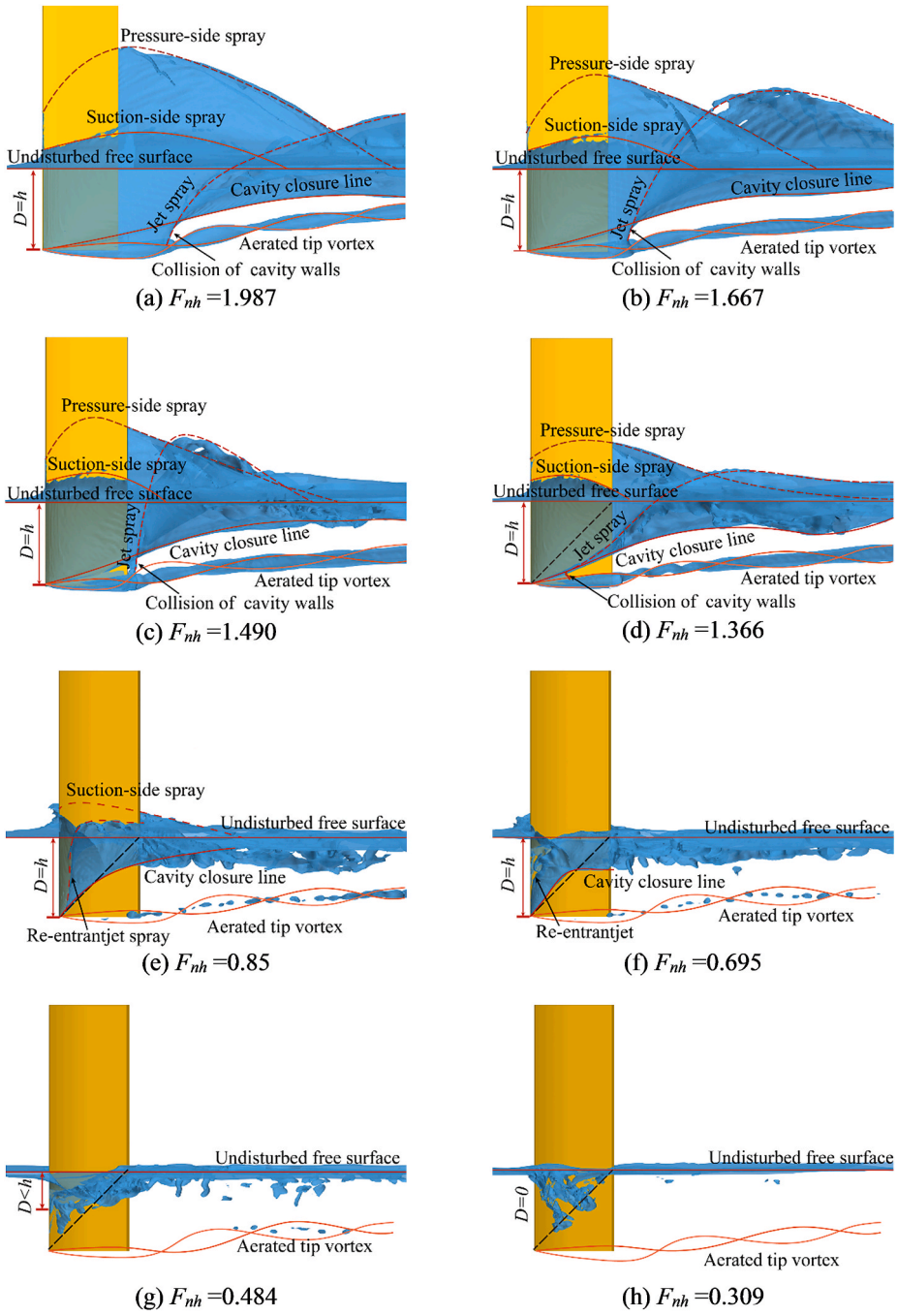

Fig. 9. Evolution of ventilated cavity shape during the deceleration process.

ventilation cavity cannot reach the free tip of the hydrofoil and the re-entrant jet significantly affects the leading edge. As the Froude number constantly decreases, some ventilated cavities underwater are reattached by the liquid water, and there is no connection between the ventilated cavity and the free surface. The ventilated cavity starts to shed off along the streamwise direction and the hydrofoil suction surface finally transits to FW state.

4.3. Vortical structures

The vortex structure around the hydrofoil is of great significance to study ventilation elimination. The Q criterion (Hunt et al., 1988) can visualize the spatial structure of the vortex in the flow field and give a better understanding of the vortex evolution during the hydrofoil decelerates. Q is defined as follows:

$$Q = -\frac{1}{2}\left[\left(\frac{\partial u}{\partial x}\right)^2 + \left(\frac{\partial v}{\partial y}\right)^2 + \left(\frac{\partial w}{\partial z}\right)^2\right] - \left[\frac{\partial u}{\partial y}\frac{\partial v}{\partial x} + \frac{\partial u}{\partial z}\frac{\partial w}{\partial x} + \frac{\partial v}{\partial z}\frac{\partial w}{\partial y}\right] \tag{5}$$

Fig. 10 shows the evolution of the vortex structure around a surface-piercing hydrofoil during deceleration. The underwater vortex structure of the hydrofoil mainly includes the tip vortex, the unstable vortex of the shear layer, and the Karman vortex caused by the vortex shedding at the hydrofoil trailing edge.

Shear layer instabilities are associated with boundary layer separation (Stern et al., 2013) and are caused by the separation of the free surface and the ventilated cavity. Therefore, the vortex structure shape caused by shear layer instabilities is consistent with the ventilated

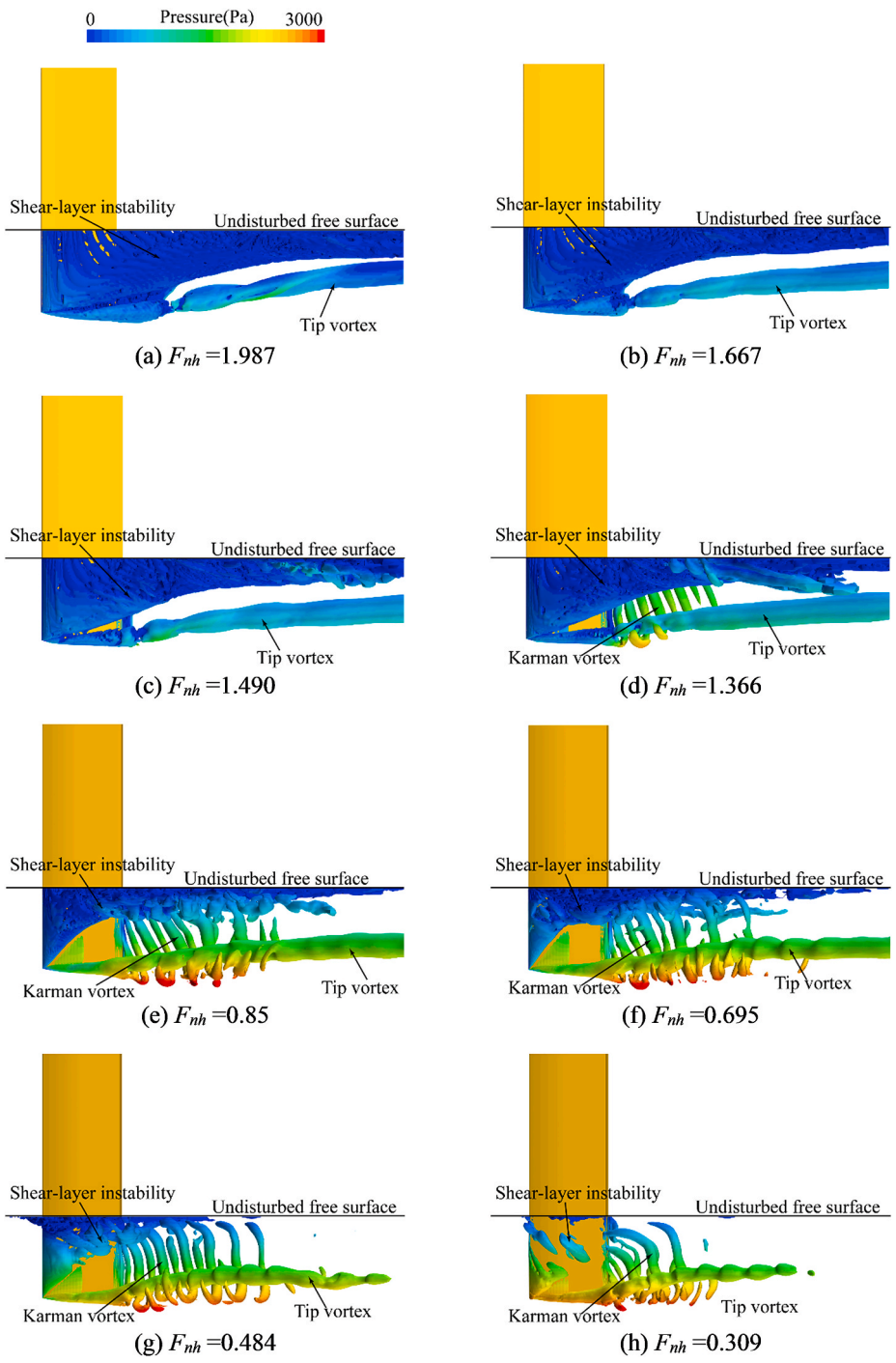

Fig. 10. Evolution of vortex structures (Q = 200 s^{-2}).

cavity. With the decrease of the ventilated cavity and water spray during the deceleration process, the vortex structure caused by shear layer instabilities becomes smaller. It is observed that the ventilated cavity surface pressure is equal to the atmospheric pressure because the ventilated cavity surface is connected to the atmosphere.

Karman vortices (Chen et al., 2020; Zhao et al., 2020) were observed for vortex shedding, which was caused by the interaction of two opposite vortices initiated by the shear layer instability at the trailing edge of the hydrofoil. The ventilated cavity affects the vortex shedding at the trailing edge. When the hydrofoil speed is high, the Karman vortex is almost invisible at the hydrofoil trailing edge. When the hydrofoil speed continues to decrease, the ventilated cavity at the hydrofoil trailing edge disappears, and the hydrofoil trailing edge forms an obvious Karman vortex with a three-dimensional effect. When the hydrofoil speed is reduced to F_{nh} = 0.309, the hydrofoil flow regime transits from PV to PW flow, the Karman vortex at the hydrofoil trailing edge decreases again owing to the small Reynolds number. When the ventilated cavity can't encapsulate the hydrofoil trailing edge, the boundary layer separation would occur on the hydrofoil due to the adverse pressure gradient, forming the shear layers. Then the two shear layers alternately roll up in opposite directions and are shed into the wake to form the vortex street (Anderson and Szewczyk, 1997). When the cavity encapsulates the hydrofoil trailing edge, one shear layer develops from the hydrofoil pressure surface, and the other shear layer forms from the cavity surface. The

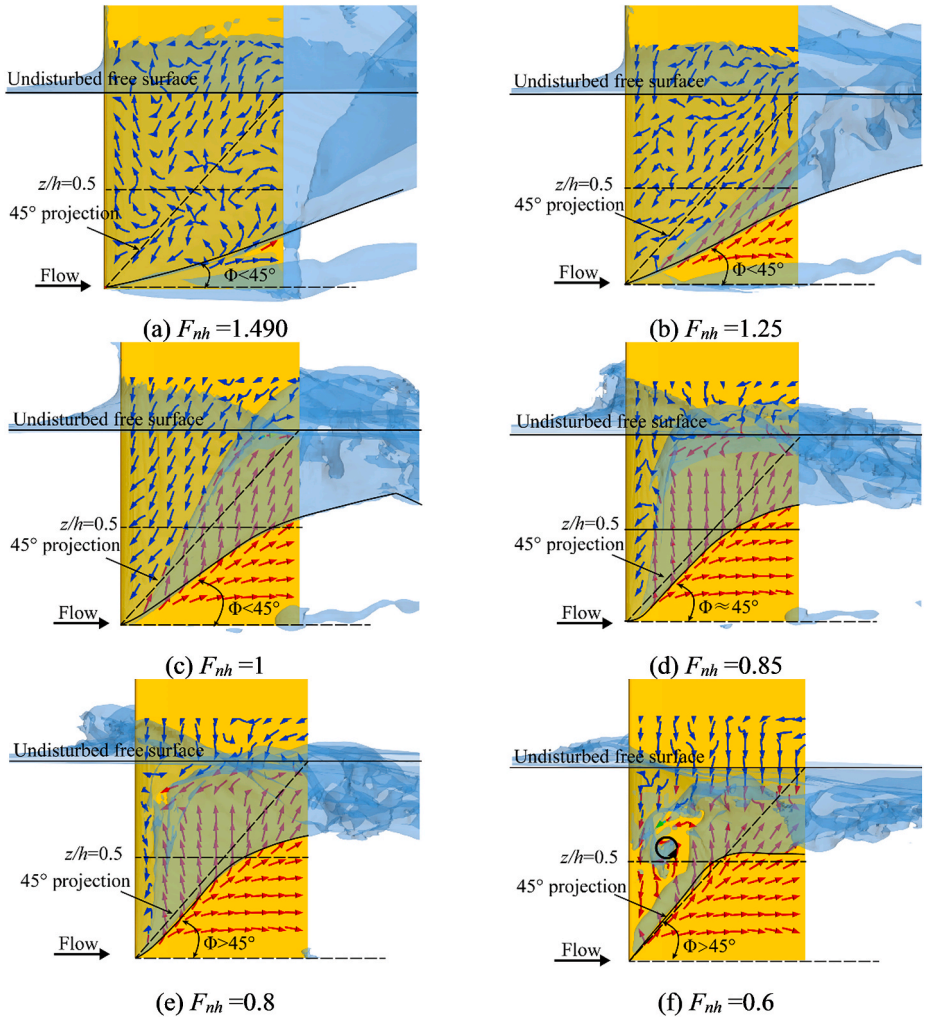

Fig. 11. Limiting streamlines on suction surface.

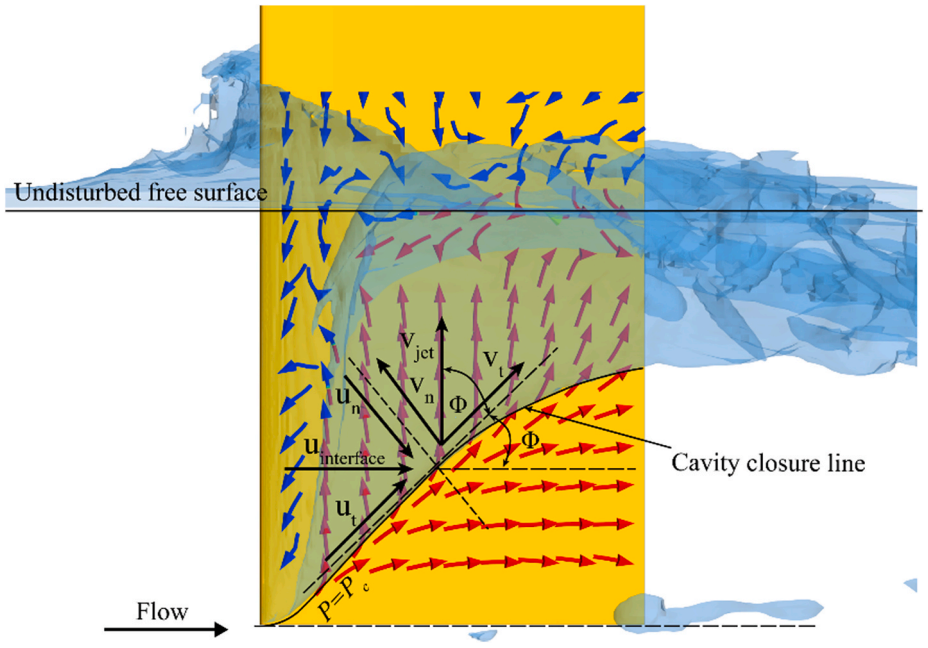

Fig. 12. Schematic diagram of the theoretical re-entrant jet.

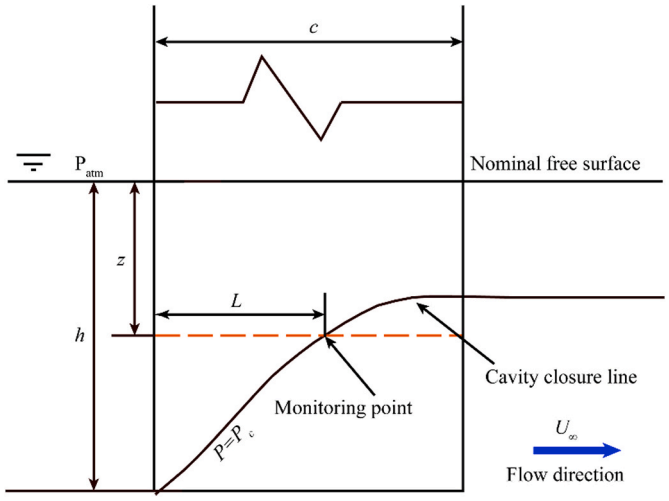

Fig. 13. Schematic diagram of the monitoring point.

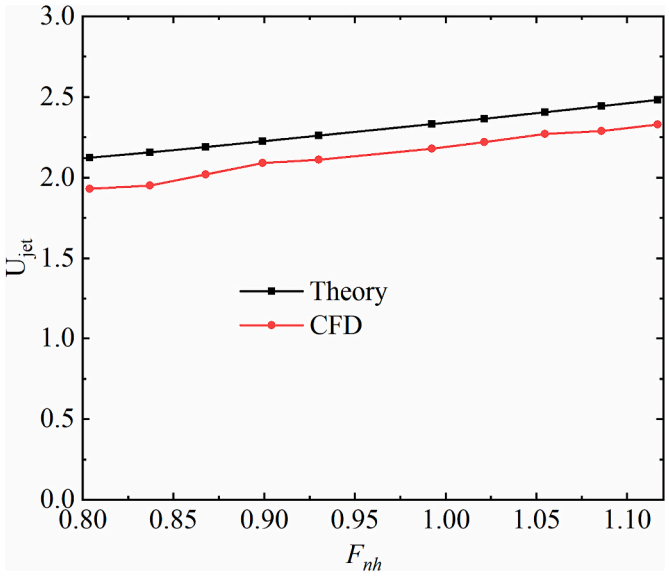

Fig. 14. Comparison of the calculated and theoretical values ($z = 0.5h$).

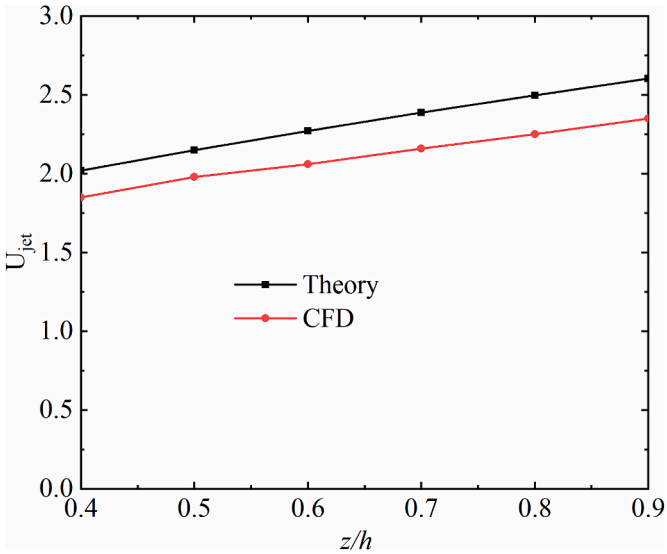

Fig. 15. Comparison of the calculated and theoretical values ($F_{nh} = 0.85$).

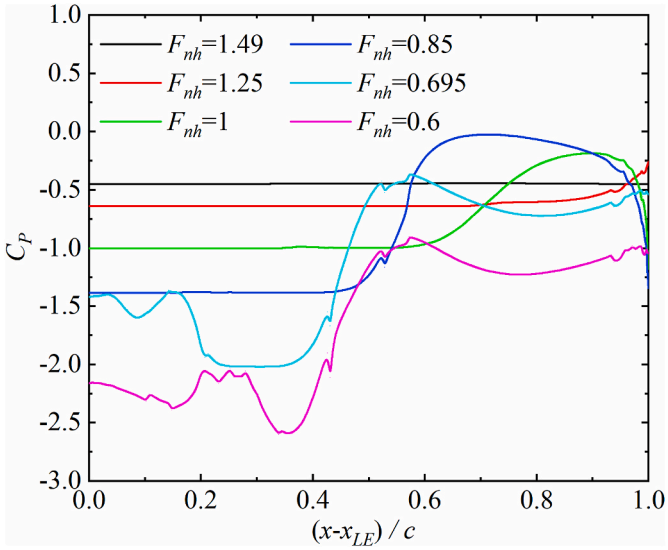

Fig. 16. Pressure coefficient distribution of suction surface ($z = 0.5h$).

ventilated cavity surface prevents the roll-up of the shear layer (Wang et al., 2021).

The tip vortex is related to the hydrofoil speed and the ventilated cavity shape. Under the high-speed condition, the core of the tip vortex is aerated by air from the ventilated cavity. As the hydrofoil speed decreases, the core of the tip vortex can't be aerated by air from the ventilated cavity, the tip vortex gradually decreases.

4.4. Re-entrant jet mechanisms

Fig. 11 shows limiting streamlines on the hydrofoil suction surface for different Froude numbers. Blue arrows indicate the gas flow trajectory in the ventilated cavity, and red arrows indicate the water flow trajectory and the re-entrant jet, respectively. It can be seen that the direction of the re-entrant jet is closely related to the ventilated cavity shape. $\Phi = 45°$ is the criterion for the stability of fully ventilated cavities (Harwood et al., 2014, 2016). When $\Phi < 45°$, the re-entrant jet moves downstream which is gradually away from the cavity's leading edge. When $\Phi > 45°$, the re-entrant jet has sufficient upstream momentum and impinges on the ventilated cavity leading edge, resulting in the inception of ventilated cavity instability. When the hydrofoil velocity is reduced, the re-entrant jet destabilizes the ventilated cavity structure at the leading edge and forms a vortex, cutting off part of the ventilated cavity and detaching downstream.

Fig. 12 shows a schematic diagram of the theoretical re-entrant jet. For a ventilated cavity on the suction surface, a concave re-entrant jet is formed, forcing the water into the ventilated cavity. The ventilated cavity length shows a non-uniform distribution in the hydrofoil spanwise direction, which demonstrates obvious three-dimensional flow features. Pressure at the boundary of the ventilated cavity is constant (De Lange and De Bruin, 1997; Wilcox, 1998), and re-entrant jet velocity is equal to inflow velocity along with the cavity interface according to the Bernoulli equation (De Lange and De Bruin, 1997; Franc and Michel, 2006). Supposing inflow velocity is represented by the normal and tangential components on the ventilated cavity's closure line. In that case, according to the momentum conservation, the tangential component of the re-entrant jet velocity has the same magnitude as the tangential component of the inflow velocity along the cavity closure line. It can be seen from Fig. 12 that when $\Phi > 45°$, the re-entrant jet points toward the leading edge of the hydrofoil. When the jet has sufficient upstream momentum, it will impinge on the leading edge of the

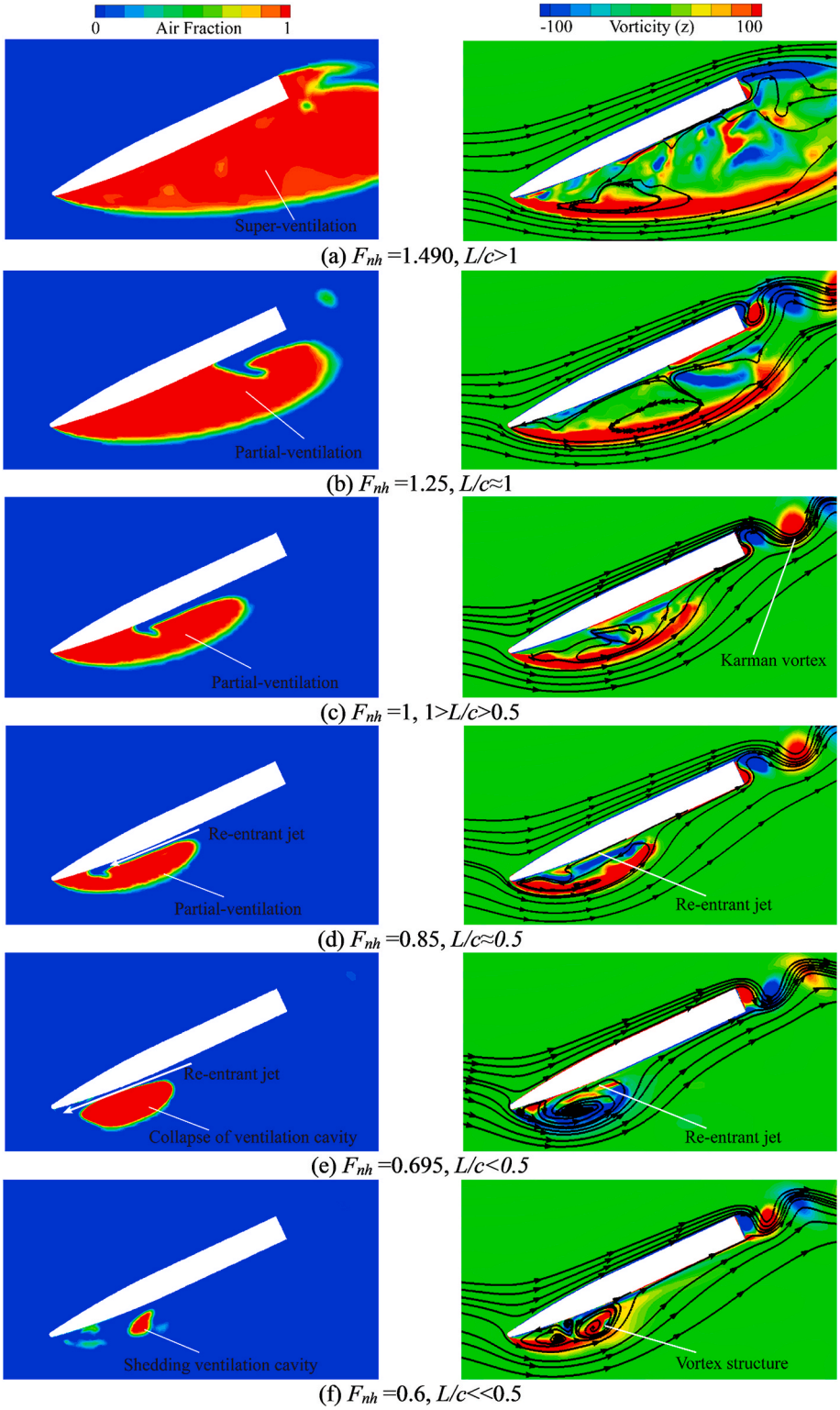

Fig. 17. Ventilated cavity and vorticity distribution($z = 0.5h$).

ventilated cavity and destabilize it. When $\Phi < 45°$, the re-entrant jet points downstream, away from the leading edge of the ventilated cavity, and thus the ventilated cavity has enough energy to remain stable.

Fig. 13 shows a schematic diagram of the monitoring point. The monitoring point is the longest position of the two-dimensional ventilated cavity of the hydrofoil with different immersion depths, where z is the immersion depth of the monitoring point, L is the ventilated cavity length, P_c is the pressure of the ventilated cavity ($P_c = P_{atm}$) (De Lange and De Bruin, 1997; Wilcox, 1998). The immersion depth Froude number of the monitoring point can be defined by:

$$F_{nh} = \frac{U_\infty}{\sqrt{gh}} \tag{6}$$

The cavitation number of the monitoring point is defined by :

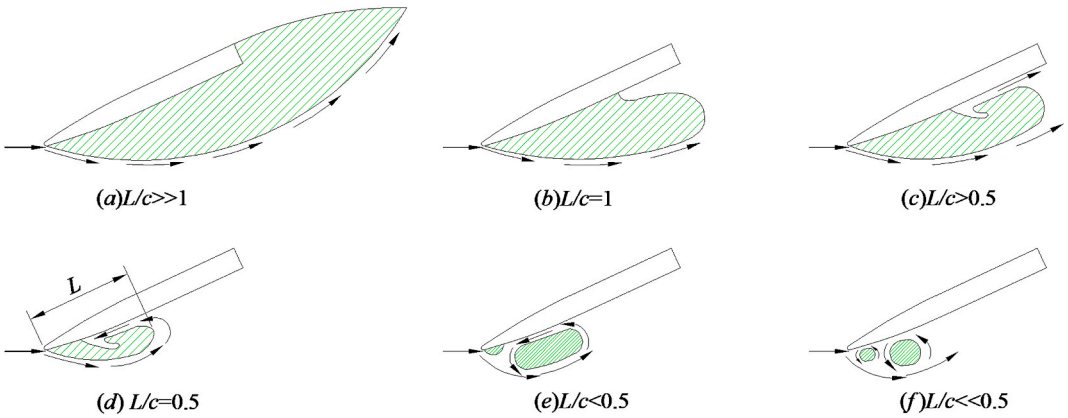

Fig. 18. Evolution of the ventilated cavity($z = 0.5h$).

$$\sigma_c = \frac{P_\infty - P_c}{0.5\rho U_\infty^2} = \frac{P_{\text{atm}} + \rho g z - P_c}{0.5\rho U_\infty^2} = \frac{P_{\text{atm}} - P_c}{0.5\rho U_\infty^2} + \frac{\rho g z}{0.5\rho U_\infty^2} \tag{7}$$

$$\sigma_c = \triangle\sigma + \frac{2}{F_{nh}^2}\frac{z}{h} = \frac{2}{F_{nh}^2}\frac{z}{h} \tag{8}$$

The velocity along the streamline forming the boundary of a gaseous cavity (and therefore the velocity of the re-entrant jet) can be obtained from Bernoulli's equation:

$$U_{\text{jet}} = U_\infty\sqrt{1+\sigma_c} \tag{9}$$

By substituting Equation (8) into Equation (9), the velocity of the re-entrant jet of the monitoring point can be simplified as:

$$U_{\text{jet}} = F_{nh}\sqrt{gh}\sqrt{1+\frac{2}{F_{nh}^2}\frac{z}{h}} \tag{10}$$

Fig. 14 compares the calculated and theoretical values (Equation (10)) at the monitoring point ($z = 0.5h$) for various speeds, while Fig. 15 compares the values at different immersion depths ($F_{nh} = 0.85$). It shows that the calculated values are in good agreement with the theoretical values, indicating that the calculated re-entrant jet is consistent with its theoretical flow state. The discrepancy observed in Figs. 14 and 15 is attributed to the effects of fluid viscosity, which are not considered in the theoretical prediction.

Fig. 16 shows the pressure coefficient distribution along the hydrofoil suction surface ($z = 0.5h$) at different speeds. It can be seen that pressure is equal to atmospheric pressure when the hydrofoil is fully ventilated. As the hydrofoil speed decreases, the length of the ventilation cavity decreases and the pressure in the reattachment region increases. Simultaneously, the pressure distribution becomes more complicated due to the effect of the re-entrant jet. The pressure coefficient C_p is defined as $C_p = (P - P_\infty)/\frac{1}{2}\rho U_0^2$, where P_∞ is the far field pressure, P is the static pressure at the point, U_∞ is hydrofoil speed and ρ is water density. In that case, a cavity would occur approximately where $\sigma = -C_p$, with σ defined as in equation (7).

In order to further study the effect of the re-entrant jet on the ventilated cavity, cavity ventilation and vorticity distribution around the hydrofoil at an immersion depth of $z = 0.5h$ were extracted from the numerical simulations, as shown in Fig. 17. In the vorticity distribution contours, the blue color represents the vorticity in the clockwise direction, and the red color means the vorticity in the counterclockwise direction. As the hydrofoil speed decreased, the hydrofoil ventilated cavity ($z = 0.5h$) changed from FV to PV. When the length of the ventilated cavity was half of the hydrofoil's chord length, the re-entrant jet began to appear, corresponding to $\Phi = 45^\circ$ for the three-dimensional hydrofoil. The re-entrant jet acts on the hydrofoil leading edge to form a strong vortex structure at the leading edge, and then the attached cavity is shed off from the hydrofoil surface and rolled into the bubbly vortex structure downstream.

Fig. 18 diagrams the evolution of the ventilated cavity($z = 0.5h$), which can be described as a four-part process.

(1) A decrease in the ventilated cavity: With a decrease in hydrofoil speed, the cavitation number increases and the ventilated cavity length decreases.
(2) Development of re-entrant flow: the re-entrant jet begins to form when the length of the ventilated cavity is reduced to half the length of the hydrofoil ($L/c = 0.5$), corresponding to $\Phi = 45^\circ$. When $\Phi < 45^\circ$, the re-entrant jet points downstream, away from the leading edge of the ventilated cavity. When $\Phi > 45^\circ$, the re-entrant jet points toward the hydrofoil leading edge and migrates from the cavity's trailing edge to its leading edge.
(3) Cavity shedding: The re-entrant jet reaches the cavity near the hydrofoil leading edge and impinges on the cavity interface, pinching off the attached cavity and causing it to be shed downstream into a bubbly vortex structure (Franc and Michel, 2006). A complex vortex structure is formed around the ventilated cavity, which is caused by the interaction between the re-entrant jet and the mainstream.
(4) Reattachment: As the cavity detaches from the hydrofoil and moves downstream, the liquid water reattaches to the hydrofoil surface, and the entire process of the ventilation washout comes to an end.

5. Conclusions

The ventilation elimination of a surface-piercing hydrofoil is investigated using the RANS method coupling with a VOF model. The ventilation elimination mechanism is discussed from the perspectives of hydrofoil hydrodynamic performance, the evolution of ventilated cavities, vortex structure, and re-entrant jets. The main conclusions are as follows:

(1) The predicted lift and drag are in good accordance with the experiments, and the flow features are also well captured by the present numerical simulations.
(2) Ventilation elimination includes three stages, i.e. a decrease in the ventilated cavity, washout and reattachment. The decrease in the ventilated cavity is due to the decrease of the hydrofoil speed in the FV flow, and the ventilated cavity is relatively stable during this stage. Washout is the transition from FV to PV flow, and the ventilated cavity is relatively stable during this process. Reattachment is the transition from PV to FW flow, and the ventilated cavity is unstable during this process.

(3) The underwater vortex structures around the surface-piercing hydrofoil are composed of a tip vortex, an unstable vortex induced by the shear layer, and a Karman vortex. Shear layer instabilities are associated with boundary layer separation and are caused by the separation of the free surface and the ventilated cavity. Karman vortices were observed for vortex shedding, which was caused by the interaction of two opposite vortices initiated by the shear layer instability at the hydrofoil's trailing edge. The core of the tip vortex is aerated by ingesting air from the ventilated cavity.

(4) Ventilation stability strongly depends on the re-entrant jet. When $\Phi > 45°$, the re-entrant jet points toward the leading edge of the hydrofoil. The re-entrant jet impinges on the ventilated cavity's leading edge with sufficient upstream momentum and de-stabilizes the cavity ventilation. When $\Phi < 45°$, the direction of the re-entrant jet points downstream, and the ventilated cavity has enough energy to remain stable.

CRediT authorship contribution statement

Yuchang Zhi: Conceptualization, Investigation, Writing – original draft. **Jiemin Zhan:** Writing – review & editing, Supervision. **Renfang Huang:** Writing – review & editing, Visualization. **Rundi Qiu:** Investigation, Validation. **Yiwei Wang:** Funding acquisition, Supervision, Resources.

Declaration of competing interest

The authors declare that they have no known competing financial interests or personal relationships that could have appeared to influence the work reported in this paper.

Acknowledgments

The authors would like to gratefully acknowledge the National Natural Science Foundation of China (No. 52006232, 11772340), the Youth Innovation Promotion Association CAS (Y201906).

References

Anderson, E., Szewczyk, A., 1997. Effects of a splitter plate on the near wake of a circular cylinder in 2 and 3-dimensional flow configurations. Exp. Fluid 23 (2), 161–174.
Andrun, M., Blagojević, B., Bašić, J., Klarin, B., 2021. Impact of CFD simulation parameters in prediction of ventilated flow on a surface-piercing hydrofoil. Ship Technol. Res. 68 (1), 1–13.
Arndt, R., Hambleton, W., Kawakami, E., Amromin, E., 2009. Creation and maintenance of cavities under horizontal surfaces in steady and gust flows. J. Fluid Eng. 131 (11).
Ashworth Briggs, A., Fleming, A., Ojeda, R., Binns, J., 2014. Tracking the Vortex Core from a Surface-Piercing Foil by Particle Image Velocimetry (PIV) Using Fluorescing Particles, 19th Australasian Fluid Mechanics Conference, pp. 1–4.
Barden, T., Binns, J., 2012. On the Road to Establishing Ventilation Probability for Moth Sailing Dinghies, 18th Australasian Fluid Mechanics Conference, pp. 1–4.
Brizzolara, S., Federici, A., 2011. Super-Cavitating profiles for ultra high speed hydrofoils: a hybrid CFD design approach. In: Proc. Of HSMV2011, 9th Symposium on High Speed Marine Vehicles. Royal Institution of Naval Architects, Naples, Italy.
Brizzolara, S., Villa, D., 2012. Three phases RANS calculations for surface-piercing super-cavitating hydrofoils. In: Proceedings of the 8th International Symposium on Cavitation CAV2012. Paper, Singapore.
Brizzolara, S., Young, Y.L., 2012. Physical and theoretical modeling of surface-piercing hydrofoils for a high-speed unmanned surface vessel. In: International Conference on Offshore Mechanics and Arctic Engineering. American Society of Mechanical Engineers, pp. 831–837.
Califano, A., Steen, S., 2009. Analysis of different propeller ventilation mechanisms by means of RANS simulations. Proc. First Int. Symp. Mar. Propuls.
Charlou, M., Wackers, J., 2019. Numerical simulation of bi-stable ventilated flows around surface-piercing hydrofoils, 22th Numerical Towing Tank Symposium. NUTTS 19.
Chen, S., Zhao, W., Wan, D., 2020. CFD Study of Free Surface Effect on Flow Around a Surface-Piercing Cylinder, the Fourteenth ISOPE Pacific/Asia Offshore Mechanics Symposium. International Society of Offshore and Polar Engineers.
Damley-Strnad, A., Harwood, C.M., Young, Y.L., 2019. Hydrodynamic Performance and Hysteresis Response of Hydrofoils in Ventilated Flows, Sixth International Symposium on Marine Propulsors (SMP'19).
De Lange, D., De Bruin, G., 1997. Sheet cavitation and cloud cavitation, re-entrant jet and three-dimensionality. Appl. Sci. Res. 58 (1), 91–114.
Franc, J.-P., Michel, J.-M., 2006. Fundamentals of Cavitation. Springer science & Business media.
Harwood, C.M., Brucker, K.A., Miguel, F., Young, Y.L., Ceccio, S.L., 2014. Experimental and numerical investigation of ventilation inception and washout mechanisms of a surface-piercing hydrofoil. In: Proceedings of the 30th Symposium on Naval Hydrodynamics. Hobart, Tasmania.
Harwood, C.M., Felli, M., Falchi, M., Ceccio, S.L., Young, Y.L., 2019. The hydroelastic response of a surface-piercing hydrofoil in multi-phase flows. Part 1. Passive hydroelasticity. J. Fluid Mech. 881, 313–364.
Harwood, C.M., Felli, M., Falchi, M., Garg, N., Ceccio, S.L., Young, Y.L., 2020. The hydroelastic response of a surface-piercing hydrofoil in multiphase flows. Part 2. Modal parameters and generalized fluid forces. J. Fluid Mech. 884.
Harwood, C.M., Young, Y.L., Ceccio, S.L., 2016. Ventilated cavities on a surface-piercing hydrofoil at moderate Froude numbers: cavity formation, elimination and stability. J. Fluid Mech. 800, 5.
Hunt, J.C.R., Wray, A.A., Moin, P., 1988. Eddies, Streams, and Convergence Zones in Turbulent Flows. Center for Turbulence Research Report CTR-S88, p. 193.
Korulla, M., Sha, O., 2012. Artificially ventilated conventional hydrofoils–An experimental investigation. Int. Shipbuild. Prog. 59 (3–4), 129–162.
Matveev, K.I., Wheeler, M.P., Xing, T., 2018. Simulations of an Air-Ventilated Strut Crossing Water Surface at Variable Yaw Angles, Fluids Engineering Division Summer Meeting. American Society of Mechanical Engineers. V003T020A002.
Matveev, K.I., Wheeler, M.P., Xing, T., 2019. Numerical simulation of air ventilation and its suppression on inclined surface-piercing hydrofoils. Ocean Eng. 175, 251–261.
Metcalf, B., Longo, J., Ghosh, S., Stern, F., 2006. Unsteady free-surface wave-induced boundary-layer separation for a surface-piercing NACA 0024 foil: towing tank experiments. J. Fluid Struct. 22 (1), 77–98.
Rood Jr., E.P., 1975. Turning Maneuver Limitations Imposed by Sudden Strut Side Ventilation on a 200-Ton 80-Knot Hydrofoil Craft. DAVID W TAYLOR NAVAL SHIP RESEARCH AND DEVELOPMENT CENTER BETHESDA MD SHIP.
Roache, P.J., 1997. Quantification of uncertainty in computational fluid dynamics. Annu. Rev. Fluid Mech. 29 (1), 123–160.
Rothblum, R.S., 1977. Investigation of Methods of Delaying or Controlling Ventilation on Surface Piercing Struts. University of Leeds.
Shen, Y.T., Wermter, R., 1979. Recent studies of struts and foils for high-speed hydrofoils. Ma. Tech. Sname news 16, 71–82, 01.
Stern, F., Wilson, R., Shao, J., 2006. Quantitative V&V of CFD simulations and certification of CFD codes. Int. J. Numer. Methods Fluid. 50 (11), 1335–1355.
Stern, F., Yang, J., Wang, Z., Sadat-Hosseini, H., Mousaviraad, M., Bhushan, S., Xing, T., 2013. Computational ship hydrodynamics: nowadays and way forward. Int. Shipbuild. Prog. 60 (1–4), 3–105.
Tulin, M.P., Burkart, M., 1955. Linearized Theory for Flows about Lifting Foils at Zero Cavitation Number. DAVID TAYLOR MODEL BASIN, WASHINGTON DC.
Ungureanu, C., Lungu, A., 2010. Numerical studies on free surface flow around a hydrofoil mounted on a plate. In: AIP Conference Proceedings. American Institute of Physics, pp. 115–118.
Vernengo, G., Bonfiglio, L., Gaggero, S., Brizzolara, S., 2016. Physics-based design by optimization of unconventional supercavitating hydrofoils. J. Ship Res. 60 (4).
Wang, L., Guo, C., Xu, P., Su, Y., 2018. Analysis of the performance of an oscillating propeller in cavitating flow. Ocean Eng. 164, 23–39.
Wang, Z., Liu, H., Gao, Q., Wang, Z., Wang, Y., Wang, G., Shen, L., 2021. Numerical investigation of ventilated cavitating flow in the wake of a circular cylinder. Physical Review Fluids 6 (6), 064303.
Wang, Y., Wu, X., Huang, C., 2016. Ventilated Partial Cavitating Flow Around a Blunt Body Near the Free Surface, 16th International Symposium on Transport Phenomena and Dynamics of Rotating Machinery.
Wetzel, J., 1957. Experimental Studies of Air Ventilation of Vertical Semi-submerged Bodies.
Wilcox, D.C., 1998. Turbulence Modeling for CFD. DCW industries La Canada, CA.
Xu, C., Wang, Y., Huang, C., Yu, C., Huang, J., 2017. Cloud cavitating flow that surrounds a vertical hydrofoil near the free surface. J. Fluid Eng. 139 (10).
Young, Y.L., Brizzolara, S., Binns, J., Brown, R., Bose, N., 2013. In: Binns, J., Brown, R., Bose, N. (Eds.), Numerical and Physical Investigation of a Surface-Piercing Hydrofoil, Proceedings of the Third International Symposium on Marine Propulsors SMP, Launceston, pp. 1–8.
Yousefi, A., Shafaghat, R., 2020. Numerical study of the parameters affecting the formation and growth of ventilation in a surface-piercing propeller. Appl. Ocean Res. 104, 102360.
Yuan, X., Xing, T., 2016. Hydrodynamic characteristics of a supercavitating vehicle's aft body. Ocean Eng. 114, 37–46.
Zhao, W., Wan, D., Zhao, S., 2020. CFD Simulation of Two-phase Flows Past a Surface-Piercing Circular Cylinder, the 30th International Ocean and Polar Engineering Conference. International Society of Offshore and Polar Engineers.